GEOPHYSICS, VOL. 89, NO. 2 (MARCH-APRIL 2024); P. N45–N57, 28 FIGS.
10.1190/GEO2022-0432.1

DOI:10.1190/geo2022-0432.1

Stratal surfaces honoring seismic structures and interpreted geologic time surfaces

Fu Wang[1], Xinming Wu[1], Hongliu Zeng[2], Xavier Janson[2], and Charles Kerans[2]

ABSTRACT

Seismic horizons play a significant role in reservoir model construction and sedimentary facies interpretation, providing crucial low-frequency constraints for seismic inversion. In basin and regional interpretations, the assumption that seismic reflections represent a stratigraphic surface with constant geologic time is significant for guiding seismic interpretation. This assumption may fail when applied to local reservoir scales due to common geologic time transgressions of a particular event in regular wavelet frequency. There will be inconsistencies between seismic events and stratigraphic surfaces. To address this issue and obtain relatively accurate stratal interpretations, we develop a hybrid horizon extraction method honoring seismic structures and time-stratigraphic frameworks, in which seismic reflection structures provide local details and interpreted geologic time surfaces offer critical constraints. First, we develop concepts and a workflow using a realistic outcrop model. We develop a new geology-guided structure tensor by fitting a gradient vector of seismic images and geologic time surfaces. We also consider existing geologic conditions, such as unconformities, and fuse them into our method to calculate accurate slopes and generate reliable relative geologic time images at a fine scale, followed by making slices. Further, we extend our method to 3D seismic data volumes. Our experiments, conducted using simulated and field data, show the superiority and accuracy of our hybrid method compared with the slope-based and stratal slicing methods. These results highlight the potential for applying our method to fine-scale subsurface modeling.

INTRODUCTION

Seismic horizons are critical for reservoir model construction and structure-guided seismic inversion. Using the assumption for seismic stratigraphy about the "chronostratigraphic significance of seismic reflections" (Vail et al., 1977), various methods that automatically or semiautomatically extract horizons from seismic images have been proposed. Among these methods, Stark (2003, 2004, 2005a, 2005b, 2006) first proposes to construct a relative geologic time (RGT) volume by the phase unwrapping method and converts 3D seismic data volumes to the Wheeler domain using the RGT volume. Another method generates the RGT volume by globally fitting the local slopes by solving partial differential equations (Lomask et al., 2006; Wu and Hale, 2013, 2015b; Zinck et al., 2013; Monniron et al., 2016). Recently, with the popularity of deep learning, Geng et al. (2020) and Bi et al. (2021) propose adopting a convolutional neural network to predict the RGT volume from seismic images and extract structural information from the estimated RGT. The RGT volume serves as a means of storing and retrieving seismic horizons, wherein each point contains an estimate of the geologic time (Stark, 2003). Horizons can be obtained by extracting the contour of the RGT volume. In most scenarios of regional interpretations, most automatic seismic horizon extraction methods can work well on continuous events. Even so, in areas with discontinuities or jumps (e.g., near faults and unconformities), some prior information similar to fault throws (Wu et al., 2016; Xue et al., 2018), multigrid correlations (Wu and Fomel, 2018; Wu et al., 2022), or unconformity positions (Wu and Hale, 2015a) for slope-based methods and the phase unwrapping method (Wu and Zhong, 2012) may be required to serve as constraints for accurate RGT estimation and horizon tracking.

Manuscript received by the Editor 1 July 2022; revised manuscript received 17 October 2023; published ahead of production 30 November 2023; published online 30 January 2024.
[1]University of Science and Technology of China, Laboratory of Seismology and Physics of the Earth's Interior, School of Earth and Space Sciences, Hefei, China and University of Science and Technology of China, Mengcheng National Geophysical Observatory, Mengcheng, China. E-mail: wangfu@tongji.edu.cn; xinmwu@ustc.edu.cn (corresponding author).
[2]The University of Texas at Austin, Jackson School of Geosciences, Bureau of Economic Geology, Austin, Texas, USA. E-mail: hongliu.zeng@beg.utexas.edu; xavier.janson@beg.utexas.edu; ckerans@jsg.utexas.edu.

However, due to the band-limited effect of the wavelet, Vail et al. (1977) also point out that the chronostratigraphic significance mentioned previously ensures the errors between the seismic reflection and geologic time surface are less than 1/2 cycle. Afterward, there are some analyses about the difference between the seismically interpreted and the real geologic timelines (Aigner et al., 1989; Lawrence and Doyle, 1990; Tipper, 1993; Stafleu and Sonnenfeld, 1994; Zeng et al., 1998a, 1998b; Zeng and Kerans, 2003; Hardage et al., 2007). Significantly, compared with basin and regional interpretations, when dealing with seismic horizons at the reservoir scale, the inconsistencies between the reflection events and the geologic time surface caused by regular wavelet frequency will negatively impact the stratal interpretation. Hence, the method used to calculate the RGT volume and the local geology greatly influence the extracted details of the geologic model and the stratigraphic sequence. To overcome the geologic time transgression of reflection events, Zeng et al. (1998a, 1998b) propose a stratal slicing method to compute a stratal time volume by interpolating proportionally between several selected geologic time reflection events. This method could not be used between angular unconformities because the existence of geologic time gaps violates the proportional linear assumption in the stratal slicing method. To remedy the stratal slicing method, Ligtenberg et al. (2006) and De Groot et al. (2006) propose interpolating horizons following the geometric configuration of a simple model or using the dip-steering method for complex geometry to track horizons between sequences bounded by reference horizons. In addition to linear interpolation, they also propose other interpolation methods that parallel the upper or lower reference boundary. To tackle diverse and complex structures that existed in practice and generate more accurate stratal results, Dorn (2010, 2011) proposes a domain transform to remove all structural effects, similar to folding and salt bodies, generate vertical gaps, and close up spatial fault gaps in the stratal slice volume by using interpreted major unconformities and faulted horizons. For these stratal slicing methods, the structural interpretation and the number of reference horizons limit the resolution of domain transformation.

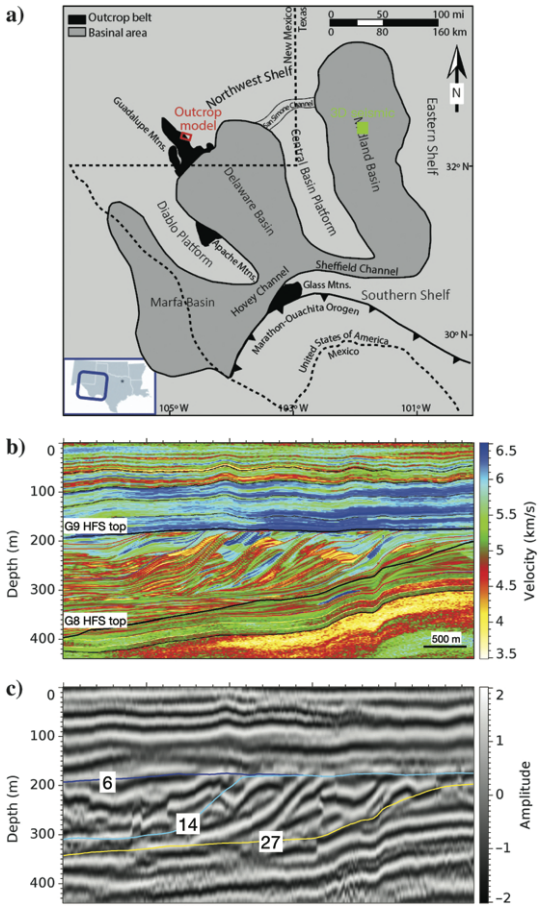

Figure 1. (a) Middle Permian paleogeography showing the Last Chance Canyon outcrop study area (the red box) and Central Basin platform subsurface study area in the Permian Basin, West Texas and New Mexico. (b) A 2D velocity model based on well and outcrop data, and (c) its corresponding synthetic seismic image. In (a), the green box represents the 3D field seismic data study area. In (c), three geologic time surfaces derived through geostatistical modeling represent known geologic time surfaces: the top 6th surface (the blue line) and the basal 27th surface (the yellow line) represent unconformities and the middle 14th surface (the green line), located between the two unconformities top-lapping with the first unconformity, represents a conformable surface. Modified from Zeng et al. (2020).

Overall, the slope-based auto-tracking methods are suitable for extracting horizons for most geologic time-equivalent seismic events but may fail to track diachronous reflection events. Stratal slicing could generate different results with the assistance of reference horizons, but it may overlook local details to some extent. Taking Zeng et al. (2020) as an example (Figure 1a–1c), for fine-scale reservoir modeling, between two angular unconformities, reflection events corresponding to thin sedimentary units with nonuniform petrophysical properties roughly match the geologic time surfaces when the analogous peak frequency of the wavelet reaches 70 Hz. The inconsistencies between seismic reflection events and geologic time surfaces increase with a decrease in frequency. Under the practical wavelet frequency, generating a reasonable and accurate stratigraphic sequence for stratal interpretation is tricky. Both the auto-tracking methods for solving partial differential equations and the stratal slicing methods have advantages and shortcomings but are complementary. The former is a data-driven method to track horizons that follow detailed seismic structures but may not be geologically reasonable. The latter is a model-driven method to extract horizons that reasonably honor prior geologic knowledge but may ignore seismic details. Combining the strengths of the two methods, a hybrid method might address this type of case more accurately and provide more accurate results than the single method alone. That motivates us to research this aspect.

In this work, we propose a workflow that combines the reflective slopes and the interpreted geologic surfaces to generate an RGT volume for stratal interpretation. Compared with the conventional slope-based method, we propose a new geology-guided structure tensor in this workflow, which integrates the normal vector estimated from reference horizons with the traditional structure tensor. In the new structure tensor, the reference horizons can provide background information about the overall stratigraphic framework, and the seismic structure can provide local details. Particularly for determining the complex unconformity structure, we select the unconformity surfaces as references. The extraordinary structural information from unconformities is also embedded in constraining the geology-guided structure tensor and the following flattening method of solving the partial differential equation.

The rest of the paper is organized as follows. We initially explain our method using 2D synthetic seismic data and three reference horizons in Figure 1c generated by Zeng et al. (2020). Subsequently, we

DOI:10.1190/geo2022-0432.1

extend our method to 3D and apply it to synthetic and field seismic data volumes. We also conduct some stratal analysis on the obtained slicing results. Finally, we compare our method with the conventional slope-based flattening and stratal slicing methods and demonstrate the advantage and potential of the proposed method for automatically and accurately interpreting detailed horizons in seismic images with limited resolution.

SEISMIC DATA

To validate the proposed method, we test our implementation in 2D and 3D cases on synthetic and field data. For the synthetic data, we select Permian mixed siliciclastic-carbonate Upper San Andres shelf-margin reservoirs (Figure 1a) as an example. The interval's shelfal stratal geometry consists of many unconformities, where many laterally continuous and vertically thin barriers exist, which challenges a previous seismic stratigraphic interpretation (He et al., 2019). We use the hybrid model built from high-resolution outcrop and subsurface data and then populate the lithostratigraphic and acoustic properties as documented in He et al. (2019). Geostatistical interpolation used in the model construction simultaneously honors the high-resolution discrete vertical measurements, the lateral continuous constraints, and the published 3D depositional models. With the acoustic properties established from the lithofacies based on the outcrop measurements and well logs, forward acoustic-wave equation-based modeling and migration are applied to obtain the seismic response at a 35 Hz analogous peak frequency common in field data. We also test our method on 3D field seismic data located in the northwest corner of Martin County, Texas. This data set has a 28 Hz peak frequency content and images of the same stratigraphic formation and facies model. In this data, the Upper San Andres formation is characterized by a strongly southward-prograding clinoform that corresponds to the southward migration of the Upper San Andres margin in the Midland Basin (Todd, 1976; Wilson et al., 2019).

NEW HYBRID STRATAL SLICING METHOD

In this hybrid workflow, we first introduce the conventional structure tensor and the improved geology-guided structure tensor, which fuse the background information from the reference horizons. Then, we will introduce the geology-guided structure tensor and the flattening method with the constraint of reference horizons to generate an RGT.

Conventional structure tensor

A simple method of calculating seismic slope is the gradient vector. It indicates the orientation along which the seismic amplitude changes the most. As gradient is the first derivative, it is sensitive to random noise or measurement errors in seismic data, which can lead to unreliable estimation. Thus, in structural interpretation, the slope of seismic events is often estimated by fitting the dominant gradient vector of the local neighborhood in the sense of least squares. Further, this problem can be transformed into finding the eigenvector corresponding to the largest eigenvalue of the structure tensor (Van Vliet and Verbeek, 1995; Weickert, 1997; Fehmers and Höcker, 2003). This eigenvector can provide an estimate of the normal vector of seismic events. Figure 2b represents the normal vector estimated by the gradient, and Figure 2f represents that by the structure tensor. The difference between the two results is evident. As shown in Figure 1c, the top and bottom reflection events, corresponding to flat and thick sedimentary layers with uniform petrophysical properties, prefer to follow geologic surfaces (Zeng et al., 2020). In these cases, the structure tensor can provide a more stable estimation of the normal vector of the actual geologic time surfaces; however, in the middle, seismic reflection events, corresponding to complex geologic structures and lithologic variation, do not align with geologic time surfaces (Zeng et al., 2020). For those, the structure tensor merely estimates the normal vector of seismic events and not that of actual geologic time surfaces. If the calculated normal vector is not an accurate estimate of the normal vector of actual geologic surfaces, the subsequently generated RGT will deviate significantly from the actual situation.

Geology-guided structure tensor

We suggest using interpreted geologic time surfaces as reference horizons to remedy the inconsistencies. As shown in Figure 1c, we select three geologic time surfaces among the 40 geologic time surfaces of the synthetic model in Figure 1b as known constraints. In the three reference horizons, the top (6th) and basal (27th) surfaces represent unconformities, which separate the strata with different sedimentary characteristics; the middle (14th) surface, located between two unconformities and partially overlapping with the top (6th) unconformity surface, represents a stratigraphic surface that does not match the seismic reflection event. The normal vector of the 14th surface indicates the accurate orientation of the stratigraphic framework between the angular unconformities. To incorporate the background information provided by the reference horizons, we propose the geology-guided structure tensor. The calculation of the geology-guided structure tensor, shown in Figure 2, consists of three parts. The first part involves interpolating the normal vector of the three reference horizons to obtain the geology-guided vector field. The second part defines a geology-guided structure tensor that fits the gradient vector field of seismic images and the geology-guided vector. The third part uses the information from the unconformity surfaces to filter the geology-guided structure tensor to preserve the inconsistent structure upon and below unconformities.

Geology-guided vector field

To interpolate the normal vector of the three reference horizons, we use the closest-point distance transform (Felzenszwalb and Huttenlocher, 2012). As mentioned previously, above the top (6th) unconformity surface (denoted by the blue line in Figure 2a), seismic reflection events mainly follow geologic surfaces. The normal vector of the top (6th) unconformity surface is almost consistent with the actual normal orientations above it. Therefore, we extend the normal vector of the top (6th) surface to the region above it using the closest-point distance interpolation. Similarly, below the basal (27th) unconformity surface (denoted by the yellow line in Figure 2a), the normal vector of the basal (27th) surface is also extrapolated to the region below it in the same way. For the region between the two unconformities, we interpolate the normal vector of the residual middle (14th) surface without overlapping with the top (6th) unconformity to this region.

By dividing the entire seismic image into three parts according to the top (6th) and basal (27th) unconformities and using closest-point distance interpolation in the three parts, respectively, we extend the normal vectors of the reference horizons to the whole image.

Consequently, we obtain the geology-guided vector field **r** (Figure 2b) and its corresponding distance field **d** simultaneously. The distance field **d** is used to calculate the weight w_r of the geology-guided vector field **r**. As shown in Figure 2c, the geology-guided vector field captures some of the structural information of the stratigraphic framework.

Seismic normal vector fitting the gradient and geology-guided vector field

Once we obtain the gradient and the geology-guided vector fields, the next step is to construct a geology-guided structure tensor that fits the two vector fields. In the process of information fusion, we calculate the weight w_g (Figure 2d) of the gradient vector field based on the eigenvalues of the conventional structure tensor. The weight w_g, also known as linearity, is commonly used to measure the quality of seismic reflections (Hale, 2009). See Appendix A for specific mathematical formulas. A higher weight indicates lower anisotropy in the seismic event, whereas a lower weight suggests higher anisotropy. The geology-guided vector field is weighted by the weight w_r (Figure 2e) mentioned previously. In the region above the top (6th) horizon and below the basal (27th) horizon, seismic events provide sufficient information to interpret the stratigraphic surface, and no additional constraints are needed. Hence, the weight w_r of the geology-guided vector field decays rapidly with the increase in distance in this region. However, near the middle (14th) surface, the weight w_r decays more slowly with distance. This is because the normal vector of the middle (14th) stratigraphic surface provides an essential constraint for accurately interpreting the horizons between the two angular unconformities. In practice, different decay rates can be applied near the middle (14th) surface, resulting in diverse interpretation results that offer valuable insights into the stratal interpretation.

Further, it is essential to note that this progress involves Gaussian-weighted fitting within a local neighborhood. As a result, the orientation estimated by the geology-guided structure tensor is smoothed around the unconformities.

A nonstationary (spatially varying) filter

In seismic stratigraphic interpretation, an unconformity is recognized as a sequence boundary where depositional terminations cause truncations, toplaps, onlaps, or downlaps. Thus, an isotropic Gaussian filter in a geology-guided structure tensor is unsuitable for dealing with unconformities. Instead, we consider unconformities as a constraint and use a nonstationary filter, as described in Wu and Hale (2015a). As an edge-preserving smoothing filter, it does not smooth across the unconformity and ensures that the different structure information below and above the unconformity is preserved.

As shown in Figure 2f and 2g, the normal vector obtained from the geology-guided structure tensor with a nonstationary filter exhibits a significant difference compared with the normal vector derived from the conventional structure tensor. The difference arises from the inclusion of the reference horizons. In the subsequent section, the differences between using a Gaussian filter and a nonstationary filter are visible across unconformities in the view of the slope.

Seismic reflection structure orientation

Using the unit eigenvector $\mathbf{u} = (u_1, u_2)$ of a structure tensor, we can compute the reflection slopes based on the mathematical equation provided in Appendix A. Figure 3a–3c shows the slopes computed from the conventional structure tensor, the geology-guided structure tensor with a Gaussian filter, and the geology-guided structure tensor with a nonstationary filter, respectively. The differences between the three results are readily apparent. Compared with Figure 3a, the estimated slopes in Figure 3b exhibit a smoother variation. Moving from Figure 3b and 3c, where a nonstationary filter is used instead of a Gaussian filter, we can observe that the inconsistent structure

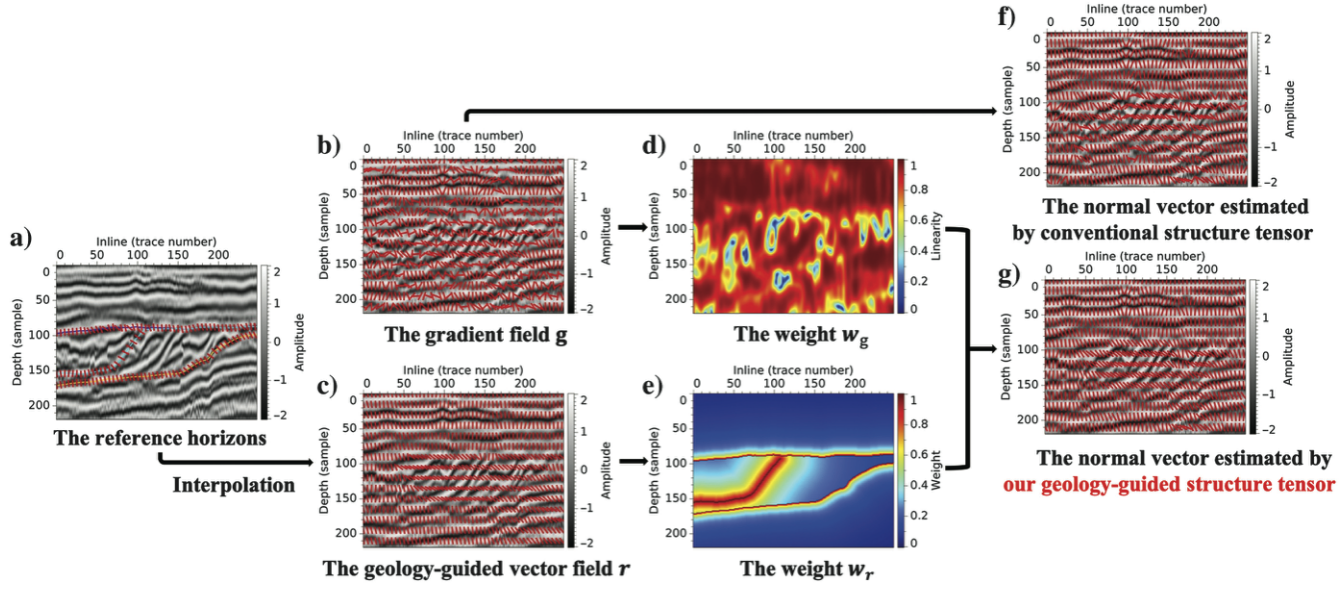

Figure 2. The pipeline of the geology-guided structure tensor. (a) The normal vector of the three reference stratal surfaces; it provides the background constraint. (b and f) The normal vector fields estimated by the gradient and the conventional structure tensor, respectively. (c) The geology-guided vector field obtained by interpolating from the normal vector of reference horizons in (a). (d and e) The weight w_g of the gradient vector field and the weight w_r of the geology-guided vector field, respectively. (g) The final result by the geology-guided structure tensor with a nonstationary filter.

below and above unconformities is effectively preserved. Using the three results to determine which is best is not persuasive. We show the three results and highlight their differences. We will give a more convincing analysis of the accuracy between the extracted horizons using different methods and the true stratigraphic surfaces for this synthetic model.

Relative geologic time

Many methods (Lomask et al., 2006; Wu and Hale, 2013, 2015b; Zinck et al., 2013; Monniron et al., 2016; Wu and Fomel, 2018) use the normal vector or slope of seismic reflectors to extract a single horizon or compute an RGT volume for the entire seismic image. The RGT volume can be converted to a horizon volume, which implicitly contains all the horizons in the seismic image. Furthermore, the horizon volume can be used to map the seismic image to the flattened image. The vertical shifts are typically continuous when generating the seismic horizon volume using these methods. However, the unconformity indicates gaps between the geologic ages. It should be incorporated into the flattening method. Here, we use the method developed by Wu and Hale (2015a) to compute reasonable discontinuous vertical shifts at unconformities. See Appendix A for specific formulas.

After obtaining the vertical shifts $s(x,t)$, we compute the corresponding RGT volume by $\tau(x,t) = t + s(x,t)$. Using the slope computed by the conventional structure tensor (Figure 3a) and the regular flattening method, we obtain an RGT volume (Figure 4a). For comparison, we use the stratal slicing method described by Zeng et al. (1998a, 1998b) to interpolate proportionally between the three reference horizons depicted in Figure 1c and obtain the corresponding RGT image (Figure 4b). Using the slope computed from the geology-guided structure tensor with a nonstationary filer (Figure 3c) and the flattening method with unconformity constraints, we achieve an RGT image (Figure 4c) that exhibits apparent discontinuities across the unconformities.

Seismic horizons

In an RGT volume, a surface with a constant τ represents a seismic horizon, regarded as a geologic time surface. As an RGT volume implicitly contains all horizons in a seismic image, it is a challenge to quantitatively analyze the errors between the horizons extracted from the three RGT volumes (as in Figure 4) and the 40 true horizons constructed from Zeng et al. (2020), as shown in Figure 5d. Here, we mainly demonstrate the position errors for the 2D test. We will give more analysis for the 3D test. For each RGT volume in Figure 4, we select 40 horizons with a minimum mean absolute error (MAE) compared with the corresponding true horizons shown in Figure 5d. The MAE is calculated as follows:

$$\mathrm{MAE}(h_e, h_t) = \frac{1}{m}\sum_{i=1}^{m} |h_e(i) - h_t(i)|, \tag{1}$$

where h_t represents a certain true horizon, h_e represents the corresponding horizon extracted from an RGT volume, and m represents the trace number of the inline profile in 2D. Figure 5a–5c shows the selected 40 horizons extracted from the corresponding RGT volumes in Figure 4a–4c, respectively. Furthermore, Figure 6 shows the MAE errors of the conventional flattening method (the blue curve), the stratal slicing method (the green curve), and our hybrid method (the red curve). These results show that all three methods exhibit small deviations and errors in the top 1st–5th and bottom 35th–40th horizons. However, in the middle part with angular unconformities, the conventional flattening method fails to extract true geologic time surfaces due to cycling skipping. The stratal slicing method behaves well for the 7th–13th horizons, where the relationship can be approximated linearly, whereas it fails to extract the 15th–25th horizons located between angular unconformities, as these do not satisfy linear assumptions. In contrast, our hybrid method shows relatively small errors. The three reference horizons provide valuable regularized information, effectively addressing the cycling skipping caused by the band-limited wavelet and complex lithologic variation. However, the drawback of our hybrid method is that it does not strictly follow reference horizons (represented as nonzero at the reference horizons in the red error curve). This is because seismic structures still have some influence in these areas. To further validate the performance of our method, we will test it on 3D synthetic and field data and provide stratal interpretations for the extracted horizons.

APPLICATION TO 3D SEISMIC DATA

Our method can be intuitively extended to 3D cases (detailed mathematical formulas are given in Appendix A). Here, we select two 3D seismic data sets to test our method: (1) synthetic seismic data (Figure 7) from the Permian Basin, West Texas and New

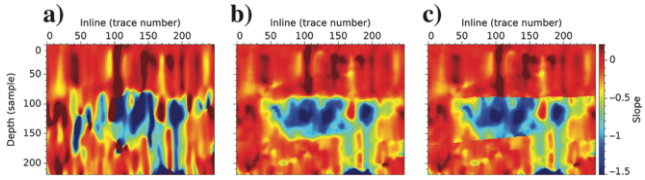

Figure 3. The slopes computed from (a) the conventional structure tensor, (b) the geology-guided structure tensor with a Gaussian filter, and (c) the geology-guided structure tensor with a nonstationary filter.

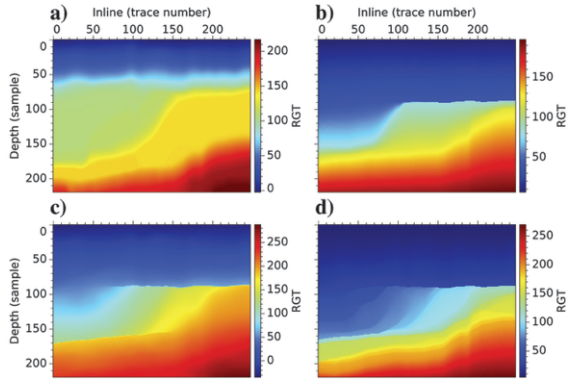

Figure 4. The RGT results calculated by different methods for the 2D synthetic case. (a) The RGT image computed from the slope of the conventional structure tensor (Figure 3a), where we apply the regular flattening method without unconformity constraints, (b) the RGT image by the stratal slicing method by interpolating proportionally between the three geologic surfaces shown in Figure 1c, (c) the RGT image computed from the slopes of the geology-guided structure tensor with a nonstationary filter (Figure 3c), where we apply the flattening method with unconformity constraints, and (d) the RGT images by interpolating between the 40 geologic surfaces shown in Figure 1b.

Mexico as depicted by the red box in Figure 1a, where one inline profile is used to explain our method in 2D (Figure 1c), and (2) a field 3D seismic data set (Figure 19) with the same subsurface stratigraphy represented by the green box in Figure 1a.

The synthetic 3D test

Figure 8a, 8c, and 8e shows the inline slopes computed from the conventional structure tensor, the geology-guided structure tensor with a Gaussian filter, and the geology-guided structure tensor with a nonstationary filter, respectively. Similarly, Figure 8b, 8d, and 8f shows the corresponding crossline slopes. In Figure 8a and 8b, we observe that the inline and crossline slopes vary rapidly, corresponding to the complex reflection events in the seismic volume. With the assistance of the reference stratigraphic surfaces shown in Figure 7, the slopes in Figure 8c and 8d are smoothed. Further, using a nonstationary filter in the geology-guided structure tensor, the estimated inline and crossline slopes in Figure 8e and 8f are discontinuous across unconformities.

Using the regular flattening method, we obtain an RGT volume in Figure 9a. Further, with the introduction of unconformity constraints in the flattening method, we obtain the corresponding RGT volume in Figure 9c. We also use the stratal slicing method and obtain the corresponding RGT image (Figure 9b). Compared with the reference RGT result in Figure 9d, the RGT volume in Figure 9c is the most plausible result, which honors both seismic structures and geologic time surfaces.

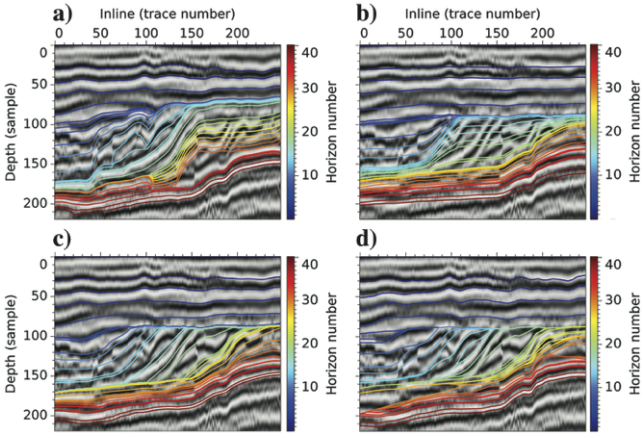

Figure 5. The extracted horizons (a–c) from the corresponding RGT volumes in Figure 4a–4c, respectively, and (d) the true horizons for the 2D synthetic data.

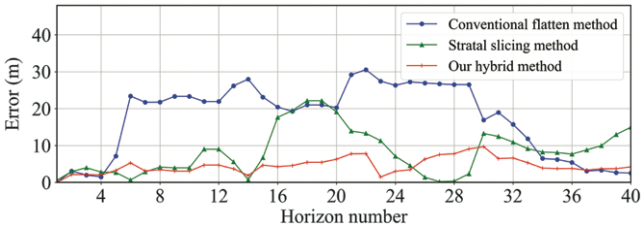

Figure 6. The errors between horizons extracted by three different methods and the true horizons. The blue, green, and red lines show the corresponding MAE between the horizons shown in Figure 5a–5d, respectively.

Taking the minimum MAE with the 40 true horizons in Figure 10d as criteria, we extract the 40 horizons (shown in Figure 10a–10c, respectively) from the three RGT volumes in Figure 9a–9c. The corresponding MAE errors are shown in Figure 11. Consistent with the 2D experiments, the accuracy of the extracted horizons varies across different parts of the seismic image. For the conventional flattening method, the top 2nd–5th and bottom 35th–40th horizons shown in Figure 10a are accurate. In the middle, where seismic events are not consistent with geologic time surfaces due to the filtering of the band-limited wavelet, the 6th–34th horizons have more significant deviations. Regarding the stratal slicing results in Figure 10b,

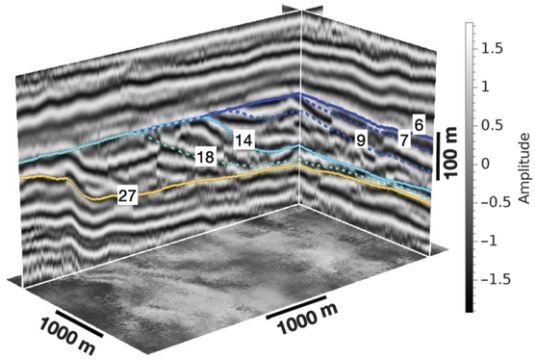

Figure 7. Synthetic 3D seismic data from the Permian Basin, West Texas and New Mexico. The three solid lines show the three geologic time surfaces, where the top 6th and basal 27th surface (the blue and green solid curves) represent unconformities, and the middle 14th surface, located between two unconformities overlapping with the first unconformity, represents a conformable surface. The three dashed lines represent the 7th, 9th, and 14th surfaces, for which we give a detailed error analysis of the three horizon extraction methods from the perspective of geologic modeling.

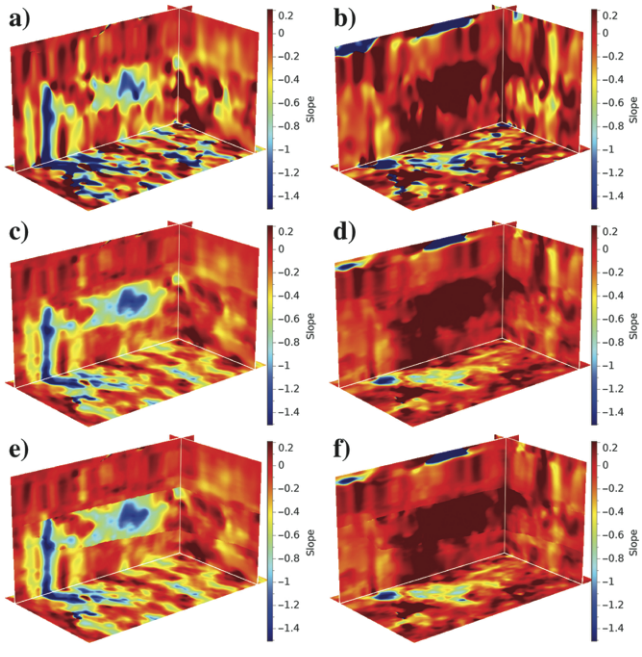

Figure 8. (a, c, and e) The inline and (b, d, and f) crossline slopes computed from (a and b) the conventional structure tensor, (c and d) the geology-guided structure tensor with a Gaussian filter, and (e and f) the geology-guided structure tensor with a nonstationary filter.

DOI:10.1190/geo2022-0432.1

only interpolating proportionally between the three reference horizons does not work well for a complex subsurface structure in the fine-scale reservoir. The results are accurate only at the reference geologic time surfaces. The 15th–26th horizons between the second and third reference horizons intersect the first unconformity interface at the same position, with some deviations from the actual geologic time surfaces. It indicates that the stratal slicing is unsuitable for interpreting in cases of angular unconformities. With many less continuous but locally time-parallel events unused, the stratal slicing method captures large-scale features but loses some local details. In contrast, our hybrid method yields horizons that are not only accurate at the top and bottom regions (the 2nd–5th and 35th–40th horizons) but also match true horizons well at the middle (the 7th–29th horizons shown in Figure 10c). Quantitatively, our method has errors that are only slightly higher than other methods in the 21st and 30th horizons. Overall, our hybrid method, fitting geologic constraints and seismic structural information, generally reduces errors and is more suitable for fine-scale reservoir modeling.

To further analyze the results in Figure 10a–10c, we show the difference in depth between the 7th, 9th, and 18th horizons of the three methods and the corresponding true horizons in Figures 12–14, respectively. The depth difference between the extracted and true horizons (also known as time-correlation error (TCE) and defined by He [2017]) contributes to distinguishing error-prone areas. It should be noted that the TCE maps shown in this paper are the shifted TCE maps. The shifted TCE map represents the relative error. In the implementation, we shift the original TCE map, which can be regarded as shifting the extracted horizon to find its optimal match with the true horizons. The optimal shift is the mean of the original TCE map. After shifting, we obtain a zero-centered TCE map and its histogram with a mean of zero and corresponding standard deviation (STD) in Figure 15. The MAE error is an absolute error. It represents the position error between two horizons. In general, if the MAE error is relatively high, the STD of the TCE map will also be relatively high. We select the MAE error to guide the horizon extraction from RGT and use the TCE map to assist further stratal interpretations. For more intuitive analysis, we also display the amplitude slicings at the 7th, 9th, and 18th horizons of the three methods in Figures 16–18, respectively.

The impact of these three different slicing approaches on geologic interpretation largely depends on the purposes of application. For high-resolution reservoir modeling guided by well picks and seismic surfaces, the TCEs of seismic surfaces (Figure 15) have significant control over the quality of the reservoir model. For geologic surfaces that are conformable (e.g., the 9th horizon) or near an unconformity (e.g., the 7th horizon), stratal slices are fairly accurate in matching true stratal surfaces with a smaller TCE (STD < 10 m or 4 ms, Figure 15b and 15e), outperforming the conventional flattening method (STD as large as 14 m or 5.6 ms, Figure 15a and 15d). For surfaces between major unconformities (especially large-angle

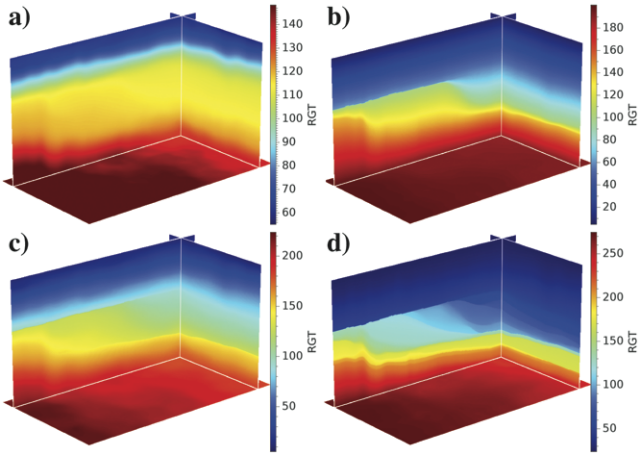

Figure 9. The RGT volumes calculated by different methods for the 3D synthetic case. (a) The RGT volume computed from the slopes of the conventional structure tensor (Figure 8a and 8b), where we apply the regular flattening method without unconformity constraints, (b) the RGT volume by the stratal slicing method by interpolating proportionally between the three geologic surfaces shown in Figure 7b, (c) the RGT volume computed from the slopes of the geology-guided structure tensor with a nonstationary filter (Figure 8e and 8f), where we apply the flattening method with unconformity constraints, and (d) the RGT volume by interpolating between the 40 geologic surfaces shown in Figure 10d.

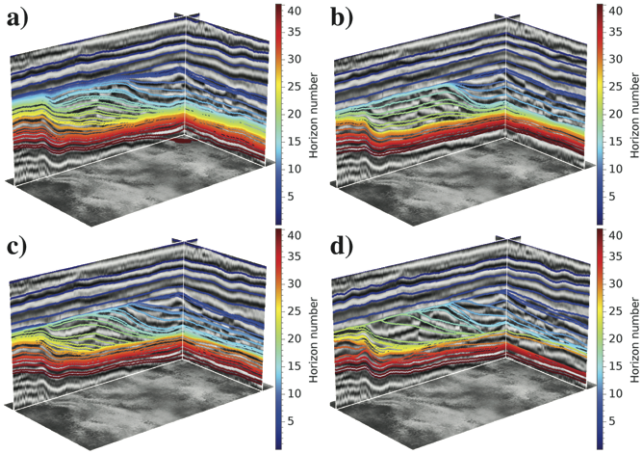

Figure 10. The extracted horizons (a–c) from the corresponding RGT volumes in Figure 9a–9c, respectively, and (d) the true horizons for the 3D synthetic data.

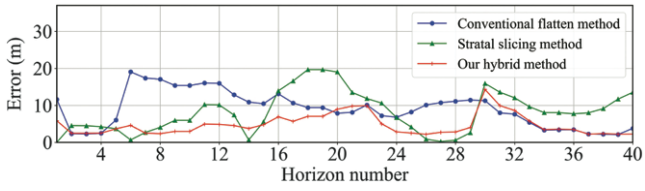

Figure 11. The errors between horizons extracted by three different methods and the true horizons. The blue, green, and red lines show the corresponding MAE between the horizons shown in Figure 10a–10d, respectively.

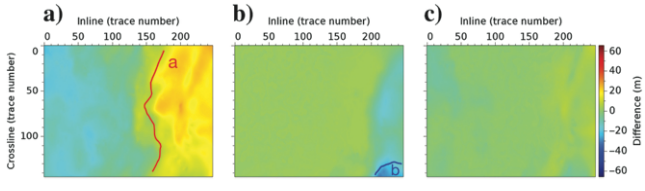

Figure 12. The difference in depth at the 7th horizon surface shown in Figure 10. (a–c) The shifted TCE maps between the 7th horizon shown in Figure 10a–10c with the true 7th stratigraphic surface shown in Figure 10d, respectively.

unconformities, for example, between the 6th and 27th horizons), stratal slicing bears a more significant error (STD of approximately 25 m or 10 ms, Figure 15h) and should be avoided, as originally recommended (Zeng et al., 1998a). Instead, a flattening surface better serves the purpose (Figure 15g). Overall, the hybrid method results in the least error and performs best (Figure 15c, 15f, and 15i).

As for the study of seismic geomorphology for depositional facies, the applicability of individual slices is determined by both TCE and the thickness of imaged lithofacies. In the outcrop model, the facies bodies (e.g., channels, reefs, and shoreface) are seismically thin-bedded (<20 m or 8 ms), and the quality of the slices is quite sensitive to TCE. For any of the three approaches, the quality of the slices is fair where the slicing error is within the ±20 m range (outside polygons, denoted as a–h2 in Figures 12–14), by roughly matching the respective seismic-geomorphologic patterns (shapes) to those on the true slice (compare Figures 16a–16c, 17a–17c, and 18a–18c to Figures 16d, 17d, and 18d, respectively). Otherwise, the quality deteriorates, and the sliced patterns fail to match the true facies patterns. In general, the flattening (auto-tracking) method tends to produce oversmoothed slices (e.g., Figures 16a, 17a, and 18a); stratal slices between large-angle unconformities (e.g., Figure 18b) bear significant errors. Again, the hybrid method is overall the best performer.

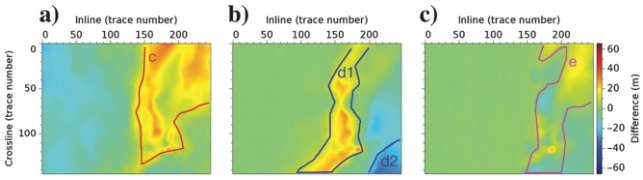

Figure 13. The difference in depth at the 9th horizon surface shown in Figure 10. (a–c) The shifted TCE maps between the 9th horizon shown in Figure 10a–10c with the true 9th stratigraphic surface shown in Figure 10d, respectively.

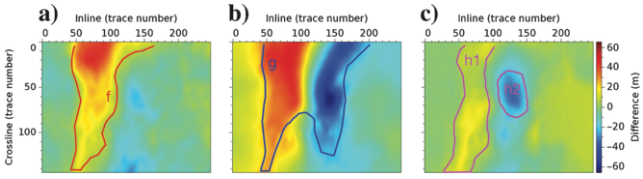

Figure 14. The difference in depth at the 18th horizon surface shown in Figure 10. (a–c) The shifted TCE maps between the 18th horizon shown in Figure 10a–10c with the true 18th stratigraphic surface shown in Figure 10d, respectively.

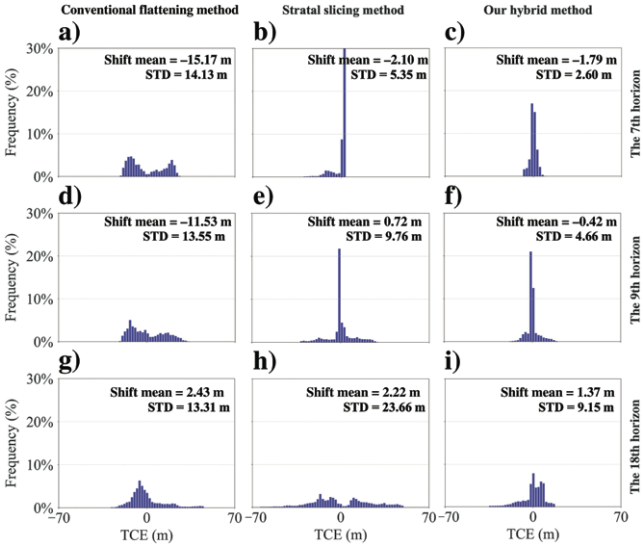

Figure 15. The histograms of the zero-centered TCE maps shown in Figures 12–14. (a–c) The histograms of the zero-centered TCE maps shown in Figure 12 for the 7th horizon surface, (d–f) the histograms of that in Figure 13 for the 9th horizon surface, and (g–i) the histograms of that in Figure 14 for the 18th horizon surface.

The field 3D test

For the field 3D seismic data volume in Figure 19, we obtain the inline and crossline slopes computed from the conventional structure tensor in Figure 20a and 20b. With the three interpreted seismic horizons (the blue, yellow, and red solid lines, denoted by the 2nd, 5th, and 6th horizons) serving as reference geologic time surfaces in Figure 19, we can obtain the inline slopes from the geology-guided structure tensor with a Gaussian filter and a nonstationary filter in Figure 20c and 20e. Figure 20d and 20f shows the corresponding crossline slopes. Compared with the slopes in Figure 20a and 20b, the slopes in Figure 20c and 20d fit the orientation information from the reference interpreted horizons. After replacing the Gaussian filter with a nonstationary filter, we observe that the inconsistencies of the slope across unconformities are clearly preserved in Figure 20e and 20f.

Figure 21a represents the RGT result by the regular flattening method. It is completely controlled by the seismic reflection dips. Figure 21b shows the RGT result using the stratal slicing method, whose trends are consistent with the three constraint surfaces. Figure 21c shows the RGT volume result using the flattening method with unconformities constraints.

Taking the minimum MAE with the seven interpreted horizons in Figure 22d as criteria, we extract seven horizons (shown in Figure 22a–22c) from the three RGT volumes in Figure 21. The corresponding MAE are shown in Figure 23. For the conventional slope-based method only fitting the seismic structure, the extracted horizons match the interpreted horizons well at the top and bottom (the 1st and 7th horizons in Figure 22a), whereas the middle three horizons (the 3rd, 4th, and 5th horizons in Figure 22a) are isolated

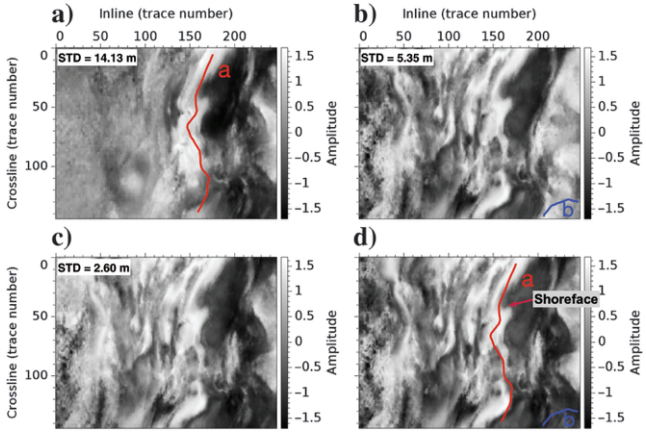

Figure 16. (a–d) The amplitude slicings of the 7th horizon surfaces corresponding to Figure 10a–10d, respectively.

and do not intersect with unconformable interfaces. This outcome is inconsistent with the interpreted horizons shown in Figure 22d. Viewing the stratal slicing results, at the bottom of the seismic image, the 7th horizon in Figure 22b is controlled by the third referent geologic surfaces. In the middle, the 3rd, 4th, and 7th horizons shown in Figure 22b intersect the first unconformity interface at the same position. This inaccurate result is caused by interpolating proportionally between the first and second interpreted geologic surfaces (the 2nd and 5th horizons) shown in Figure 19. The green error curve (Figure 23) also indicates that the errors are relatively higher than those of the other two methods in the 3rd and 4th horizons. In contrast, the horizons obtained by our hybrid method shown in Figure 22c are not only accurate at the top and bottom (the 1st and 7th horizons) but also match true horizons well in the middle, where the 3rd, 4th, and 5th horizons converge on the unconformable interface at different locations. Further, the red and blue error curves in Figure 23 indicate that adding geologic constraints in the slope-based horizon extraction methods is helpful for fine-scale stratal interpretation.

For further geologic analysis, we display the shifted TCE maps, the corresponding histograms, and the amplitude slicings at the 3rd and 5th horizon extraction results in Figures 24–28. The testing results on the field 3D data are comparable to those on the synthetic model.

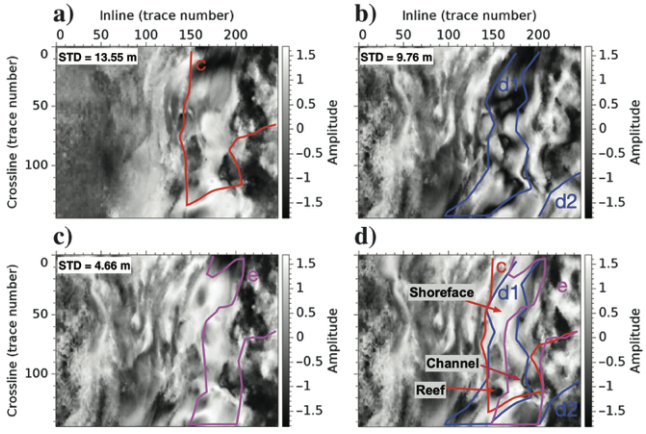

Figure 17. (a–d) The amplitude slicings of the 9th horizon surfaces corresponding to Figure 10a–10d, respectively.

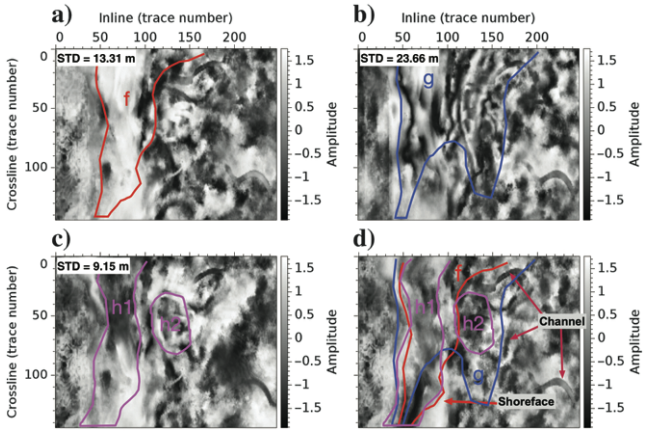

Figure 18. (a–d) The amplitude slicings of the 18th horizon surfaces corresponding to Figure 10a–10d, respectively.

Impact on high-resolution reservoir modeling depends on TCEs of seismic slices (Figure 26). For geologic surfaces that are conformable or are very close to an unconformity (e.g., the 5th horizon), stratal slices are fairly accurate in matching true stratal surfaces with small TCE (STD < 1.5 m, Figure 26e), outperforming the conventional flattening method (STD as large as 12 m or 4.8 ms, Figure 26d). For surfaces between major unconformities (e.g., between the 2nd and 5th horizons), stratal slicing bears a large error (STD approximately 15 m or 6 ms, Figure 26b) and should be avoided. Instead, a flattened surface better serves the purpose (STD = 8.09 m or 3.2 ms, Figure 26a). Again, the hybrid method produces the most minor errors and performs best (Figure 26c and 26f).

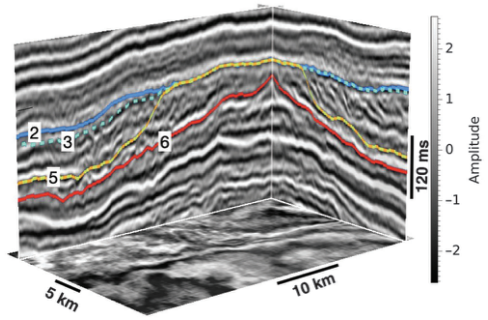

Figure 19. The 3D field seismic data. The three solid lines show the three geologic time surfaces: the 2nd and 6th surfaces (the solid blue and solid red curves) represent unconformities, and the 5th surface (the solid yellow curves), located between two unconformities overlapping with the first unconformity, represents the conformable surface. The two dashed lines represent the 3rd and 5th surfaces, for which we give a detailed error analysis for the three horizon extraction methods in terms of geologic modeling.

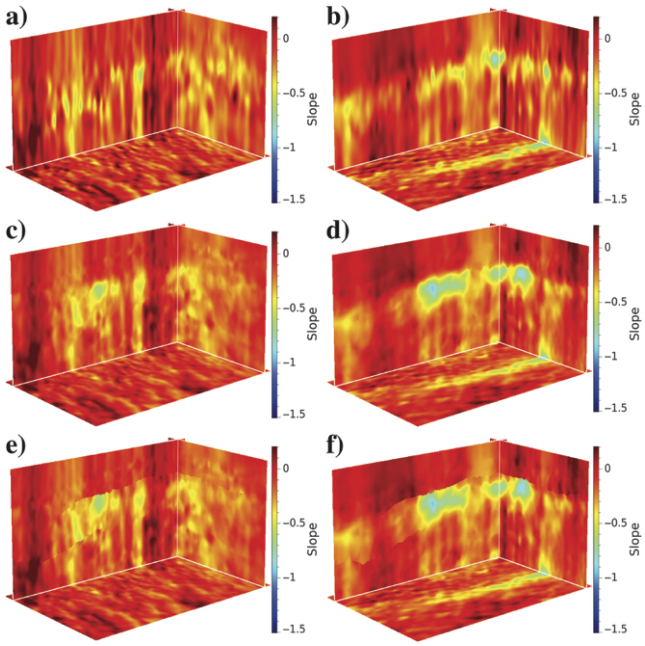

Figure 20. (a, c, and e) The inline and (b, d, and f) crossline slopes computed from (a and b) the conventional structure tensor, (c and d) the geology-guided structure tensor with a Gaussian filter, and (e and f) the geology-guided structure tensor with a nonstationary filter for the 3D field data.

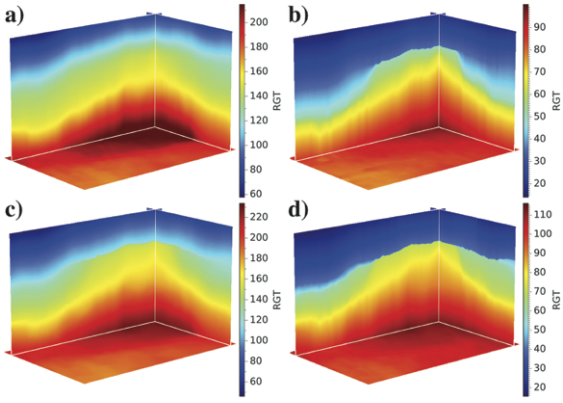

Figure 21. The RGT volumes calculated by different methods for the 3D field case. (a) The RGT volume computed from the slopes of the conventional structure tensor (Figure 20a and 20b), where we apply the regular flattening method without unconformity constraints, (b) the RGT volume by the stratal slicing method by interpolating proportionally between the three geologic surfaces shown in Figure 19, (c) the RGT volume computed from the slopes of the geology-guided structure tensor (Figure 20e and 20f) with a nonstationary filter, where we apply the flattening method with unconformity constraints, and (d) the RGT volume by interpolating between the seven geologic surfaces shown in Figure 22d.

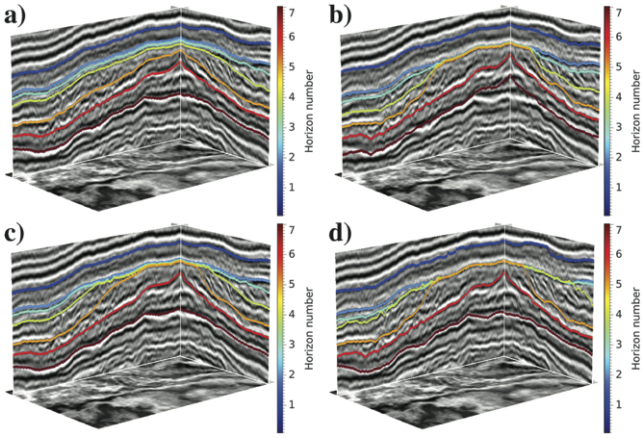

Figure 22. (a–c) The extracted horizons from the corresponding RGT volumes in Figure 21a–21c, respectively, and (d) the seven interpreted reference horizons for the 3D synthetic data.

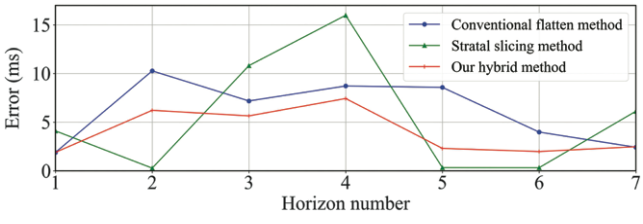

Figure 23. The errors between the horizons extracted by three different methods and the true horizons. The blue, green, and red lines show the corresponding MAE between the horizons shown in Figure 22a–22d, respectively.

For seismic geomorphology, the quality of the slices is controlled by the TCE and thickness of imaged lithofacies. The field 3D data are collected at the same stratigraphic formation with a similar facies model. The interpreted seismic facies geobodies (e.g., shelf incision, shoreface, and slope channels) should be seismically thin (<20 m or 8 ms), and their imaging is sensitive to TCE. As in this model, in any of the three approaches, the quality of the slices is acceptable where the slicing error is within the ± 10 m range (outside polygons denoted as a–f in Figures 24 and 25) by correctly imaging respective seismic-geomorphologic patterns (shapes) recorded on the true (interpreted) slice (compare Figure 27a–27c and Figure 28a–28c to Figures 27d and 28d, respectively). In other areas, the quality worsens, and the sliced patterns fail to match the true facies patterns. We observe that the flattening method produces oversmoothed slices (e.g., Figures 27a and 28a); stratal slices between large-angle unconformities (e.g., Figure 27b) bear significant error. Again, the hybrid method has the best performance.

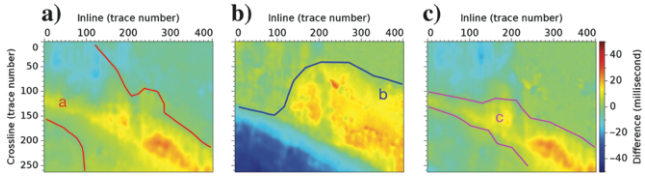

Figure 24. The difference in depth at the 3rd horizon surface shown in Figure 22. (a–c) The shifted TCE maps between the 3rd horizons shown in Figure 22a–22c with the true 3rd stratigraphic shown in Figure 22d, respectively.

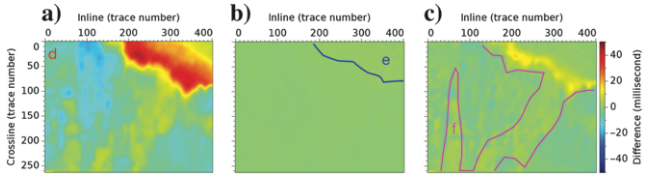

Figure 25. The difference in depth at the 5th horizon surface shown in Figure 22. (a–c) The shifted TCE maps between the 5th horizons shown in Figure 22a–22c with the true 5th stratigraphic shown in Figure 22d, respectively.

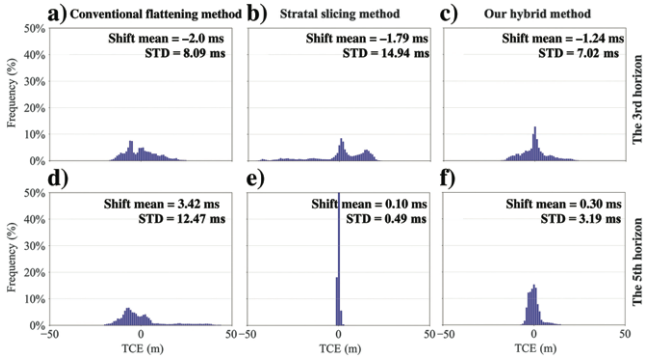

Figure 26. The histograms of the zero-centered TCE maps in Figure 24a–24c, respectively, for the 3rd horizon surface and (d–f) the histograms of that in Figure 25 for the 5th horizon surface.

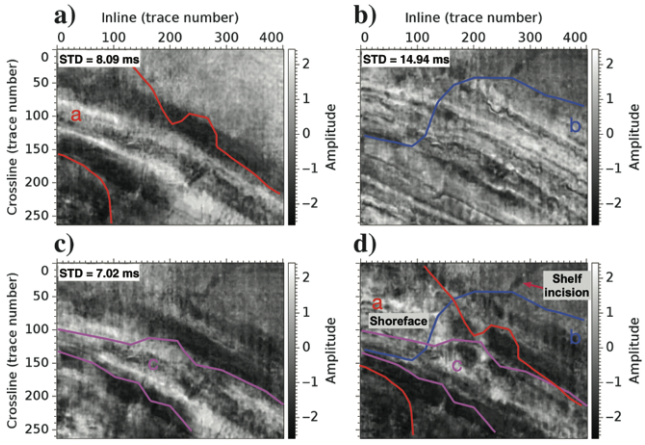

Figure 27. The amplitude slicings of the 3rd horizon surfaces, corresponding to Figure 22a–22d, respectively.

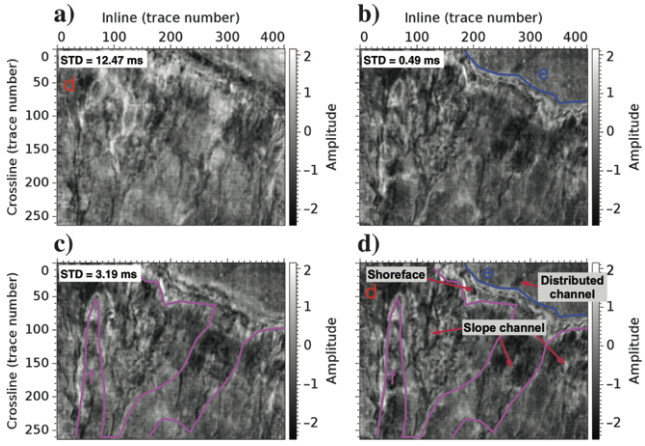

Figure 28. (a–d) The amplitude slicings of the 5th horizon surfaces, corresponding to Figure 22a–22d, respectively.

CONCLUSION

In this paper, we propose a novel horizon extraction workflow that honors both seismic reflection structures and geologic time surfaces. Our method can be used to interpret these reflection events inconsistent with the stratal surfaces caused by the limited resolution of regular wavelet and complex geologic structures. In this workflow, inspired by a conventional structure tensor, we first propose a geology-guided structure tensor to calculate the slopes. The beauty of the geology-guided structure tensor is that it deftly includes the orientation information of the reference stratal horizons. In addition, we also consider existing geologic conditions, such as unconformity, and fuse these into calculating accurate slopes and generating reliable RGT, followed by extracting horizons. The whole workflow is a combination of data-driven (slope-based) and model-driven (stratal slicing) methods in seismic stratal interpretation. The reference stratal surfaces provide crucial constraints for the complete stratigraphic framework, whereas the seismic structures offer detailed support. We choose the synthetic seismic data constructed by an outcrop model and related geology information from the Permian Basin, West Texas and New Mexico, as well as nearby field seismic data to verify our method. We also compare our hybrid method with the slope-based and stratal slicing methods. Results and further stratal interpretation in 3D synthetic and field data sets show the improvement of the extracted horizons by our new hybrid method and demonstrate that this workflow can be applied to complex subsurface data to enhance stratal and facies interpretation.

ACKNOWLEDGMENTS

Financial support for this research was provided by the National Natural Science Foundation of China (grant no. 41974121). We thank the USTC Supercomputing Center for providing computational resources for this work. We appreciate assistance from A. Masterson in polishing the language. We would like to thank the editors A. Cheng and Y. Liu, the reviewer T. Stark, and the anonymous reviewer at GEOPHYSICS for their valuable comments and suggestions that helped to improve the manuscript significantly. The authors would like to thank Geostar LCC for granting access to the field 3D seismic data for research purposes. Publication authorized by the Director, Bureau of Economic Geology.

DATA AND MATERIALS AVAILABILITY

Data associated with this research are available and can be obtained by contacting the corresponding author.

APPENDIX A

HORIZON-GUIDED SLOPES FOR SEISMIC FLATTENING

For a sample $\mathbf{y}$, we compute the normal vector $\mathbf{u}(\mathbf{x})$ by solving the following maximum problem with a constraint for the complete sample included in its neighborhood Ω:

$$\arg\max_{\mathbf{u}(\mathbf{x})} \mathbf{u}^{\top}\left(\int_{\Omega}(\mathbf{g}\mathbf{g}^{\top})G d\mathbf{y}\right)\mathbf{u} \quad \text{s.t. } \mathbf{u}^{\top}\mathbf{u}=1, \tag{A-1}$$

where $g=[\,g_1 \quad g_2\,]^T$ represents the gradient vector and $\mathbf{G}\langle\cdot\rangle$ is a Gaussian weighting function defined as the distance between the interior sample $\mathbf{y}$ of the neighborhood Ω and the centered sample $\mathbf{x}$. We abbreviate the formula as

$$\arg\max_{\mathbf{u}(\mathbf{x})} \mathbf{u}^{\top}\mathbf{T}\mathbf{u} \quad \text{s.t. } \mathbf{u}^{\top}\mathbf{u}=1, \tag{A-2}$$

where $\mathbf{T}=\int_{\Omega}(\mathbf{g}\mathbf{g}^{\top})G d\mathbf{y}$ represents the structure tensor, computed by the smoothed outer products of the neighborhood gradient vectors near $\mathbf{x}$. Based on the Lagrange multiplier method, this maximum problem with a constraint can be considered as finding a vector $\mathbf{u}$ corresponding to the extreme of the formula $\mathbf{u}^{\top}\mathbf{T}\mathbf{u}+\lambda(1-\mathbf{u}^{\top}\mathbf{u})$. Considering that this formula is the quadratic function of $\mathbf{u}$, we have $\mathrm{Tu}=\lambda\mathbf{u}$ by extracting the derivative of this function with respect to $\mathbf{u}$ and making it equal to zero. The eigenvector corresponding to the largest eigenvalue, obtained by the eigendecomposition of the structural tensor $\mathbf{T}$, is the vector $\mathbf{u}$ that maximizes the preceding quadratic objective function.

The structure tensor is a symmetric positive-semidefinite matrix of size 2×2, defined as

DOI:10.1190/geo2022-0432.1

$$\mathbf{T} = \langle \mathbf{g}\mathbf{g}^{\top} \rangle = \begin{bmatrix} \langle g_1 g_1 \rangle & \langle g_1 g_2 \rangle \\ \langle g_1 g_2 \rangle & \langle g_2 g_2 \rangle \end{bmatrix}, \tag{A-3}$$

where $\langle \cdot \rangle$ denotes Gaussian smoothing for the outer product in the angle brackets. The eigendecomposition of the structure tensor can be represented as

$$\mathbf{T} = \lambda_u \mathbf{u}\mathbf{u}^{\top} + \lambda_v \mathbf{v}\mathbf{v}^{\top}, \tag{A-4}$$

where $\mathbf{u}$ and $\mathbf{v}$ are the unit eigenvector respectively corresponding to the eigenvalue λ_u and λ_v of the structure tensor $\mathbf{T}$. Assuming $\lambda_u \geq \lambda_v$, the eigenvector $\mathbf{u}$ represents the direction along which the seismic amplitude varies the most, so it is perpendicular to the local linear reflection in the seismic image, whereas the orthogonal eigenvector $\mathbf{v}$ represents the direction with a consistent feature, in other words, parallel to the local seismic reflection.

By extending the normal vector fitting the gradient direction field to that fitting both the gradient and the geology-guided vector field, we pose the following constrained maximum problem:

$$\underset{\mathbf{u}(\mathbf{x})}{\arg\max} \mathbf{u}^{\top} \left(\int_{\Omega} (w_g \mathbf{g}\mathbf{g}^{\top} + w_r \mathbf{r}\mathbf{r}^{\top}) G d\mathbf{y} \right) \mathbf{u} \text{ s.t.} \mathbf{u}^{\top}\mathbf{u} = 1, \tag{A-5}$$

where $\mathbf{r}$ represents the geology-guided vector and w_g, and w_r respectively represent the weight of gradient vector $\mathbf{g}$ and geology-guided vector $\mathbf{r}$ in estimating the normal vector $\mathbf{u}$ of the true stratigraphic framework. In addition, the meanings of the remaining variables are the same as that in equation A-2.

Further, the geology-guided structure tensor is defined as follows:

$$\begin{aligned} \mathbf{T} &= \int_{\Omega} (w_g \mathbf{g}\mathbf{g}^{\top} + w_{\mathbf{r}} \mathbf{r}\mathbf{r}^{\top}) G d\mathbf{y} \\ &= \begin{bmatrix} \langle w_g g_1 g_1 + w_r r_1 r_1 \rangle & \langle w_g g_1 g_2 + w_r r_1 r_2 \rangle \\ \langle w_g g_1 g_2 + w_r r_1 r_2 \rangle & \langle w_g g_2 g_2 + w_r r_2 r_2 \rangle \end{bmatrix}, \end{aligned} \tag{A-6}$$

where r_1 and r_2 represent the vertical and horizontal components of the geology-guided vector, respectively. However, due to Gaussian weighting, the normal vector computed from the geology-guided structure tensor is smoothed around the unconformity. To preserve inconsistent structures above and below unconformities, we alternatively use a nonstationary filter in the geology-guided structure tensor. The constrained maximum problem and the geology-guided structure tensor with a nonstationary filter can be redefined as

$$\underset{\mathbf{u}(\mathbf{x})}{\arg\max} \mathbf{u}^{\top} \left(\int_{\Omega} (w_g \mathbf{g}\mathbf{g}^{\top} + w_r \mathbf{r}\mathbf{r}^{\top}) S d\mathbf{y} \right) \mathbf{u} \text{ s.t.} \mathbf{u}^{\top}\mathbf{u} = 1 \tag{A-7}$$

and

$$\begin{aligned} \mathbf{T} &= \int_{\Omega} (w_g \mathbf{g}\mathbf{g}^{\top} + w_r \mathbf{r}\mathbf{r}^{\top}) S d\mathbf{y} \\ &= \begin{bmatrix} \langle w_g g_1 g_1 + w_r r_1 r_1 \rangle_s & \langle w_g g_1 g_2 + w_r r_1 r_2 \rangle_s \\ \langle w_g g_1 g_2 + w_r r_1 r_2 \rangle_s & \langle w_g g_2 g_2 + w_r r_2 r_2 \rangle_s \end{bmatrix}, \end{aligned} \tag{A-8}$$

where $\mathbf{S}$ and $\langle \cdot \rangle_s$ both represent the nonstationary filter varying spatially, for which the scale of smoothing is controlled by the constraints of unconformities. The nonstationary filters here are implemented by the edge-preserving smoothing filter (Hale, 2011).

The unit eigenvector $\mathbf{u}$ of the structure tensor contains vertical and horizontal components $\mathbf{u} = (u_1, u_2)$. By assuming that the normal vectors usually point downward and the vertical component $u_1 > 0$, we can compute the reflection slopes p as follows:

$$p(\mathbf{x}) = -\frac{u_2(\mathbf{x})}{u_1(\mathbf{x})}. \tag{A-9}$$

After obtaining the seismic slopes, to preserve the gap in the geology age at the unconformity, we use the flattening method with unconformity constraints (Wu and Hale, 2015a):

$$\begin{bmatrix} w\left(-\frac{\partial s}{\partial x} - p\frac{\partial s}{\partial t}\right) \\ \epsilon \frac{\partial s}{\partial t} \end{bmatrix} \approx \begin{bmatrix} wp \\ 0 \end{bmatrix}, \tag{A-10}$$

where $p(x,t)$ represents the seismic reflector slopes, $w(x,t)$ represents the weights of the equations, and the second equation $\epsilon(\partial s/\partial t) \approx 0$ with a small constant ϵ is used to generate continuous vertical shifts. As for unconformities contained in the seismic image, unconformity can be incorporated into the preceding equations by setting $w(x,t) = 1 - g_t(x,t)$ and $\epsilon(x,t) = \epsilon_0[1 - g_t(x,t)]$, where ϵ_0 is a minuscule constant. The spatially varying $\epsilon(x,t)$, with a smaller value at unconformities, greatly benefits generating reasonable discontinuous vertical shifts at unconformities. Furthermore, unconformity can be further used to constrain the preconditioner of the conjugate gradient method in solving these equations (Wu and Hale, 2015a).

For 3D seismic data, applying the closest-point distance transform to a 3D space with three geologic time surfaces, we can also obtain the corresponding geology-guided vector field $\mathbf{r}$ and distance field $\mathbf{d}$. Then, following the same process, we can derive the geology-guided structure tensor with a nonstationary filter:

$$\begin{aligned} \mathbf{T} &= \int_{\Omega} (w_g \mathbf{g}\mathbf{g}^{\top} + w_r \mathbf{r}\mathbf{r}^{\top}) S d\mathbf{y} \\ &= \begin{bmatrix} \langle w_g g_1 g_1 + w_r r_1 r_1 \rangle_s & \langle w_g g_1 g_2 + w_r r_1 r_2 \rangle_s & \langle w_g g_1 g_3 + w_r r_1 r_3 \rangle_s \\ \langle w_g g_1 g_2 + w_r r_1 r_2 \rangle_s & \langle w_g g_2 g_2 + w_r r_2 r_2 \rangle_s & \langle w_g g_2 g_3 + w_r r_2 r_3 \rangle_s \\ \langle w_g g_1 g_3 + w_r r_1 r_3 \rangle_s & \langle w_g g_2 g_3 + w_r r_2 r_3 \rangle_s & \langle w_g g_3 g_3 + w_r r_3 r_3 \rangle_s \end{bmatrix}, \end{aligned} \tag{A-11}$$

where g_1, g_2, and g_3 represent the vertical, inline, and crossline components of the gradient vector, respectively, and r_1, r_2, and r_3 represent the vertical, inline, and crossline components of the geology-guided vector, respectively. Weight w_g is linearity computed by the conventional 3D structure tensor, and weight w_r is also calculated by the distance field $\mathbf{d}$. Clearly, $\mathbf{S}$ and $\langle \cdot \rangle_s$ also represent the nonstationary filter controlled by the unconformities.

Next, we compute inline slope $\mathbf{p}$ and crossline slope $\mathbf{q}$ based on the eigenvector $\mathbf{u} = (u_1, u_2, u_3)$ of the geology-guided structure tensor in equation A-11:

$$p(\mathbf{x}) = -\frac{u_2(\mathbf{x})}{u_1(\mathbf{x})} \quad \text{and} \quad q(\mathbf{x}) = -\frac{u_3(\mathbf{x})}{u_1(\mathbf{x})}. \tag{A-12}$$

Finally, the flattening method used in generating the seismic horizon volume with unconformities is clear:

$$\begin{bmatrix} w\left(-\frac{\partial s}{\partial x} - p\frac{\partial s}{\partial t}\right) \\ w\left(-\frac{\partial s}{\partial y} - q\frac{\partial s}{\partial t}\right) \\ \epsilon\frac{\partial s}{\partial t} \end{bmatrix} \approx \begin{bmatrix} wp \\ wq \\ 0 \end{bmatrix}, \tag{A-13}$$

where the meaning of the variables is consistent with equation A-10.

REFERENCES

Aigner, T., M. Doyle, D. Lawrence, M. Epting, and A. V. Vliet, 1989, Quantitative modeling of carbonate platforms: Some examples, *in* P. D. Crevello, ed., Controls on carbonate platforms and basin development: SEPM Society for Sedimentary Geology, 323–338.

Bi, Z., X. Wu, Z. Geng, and H. Li, 2021, Deep relative geologic time: A deep learning method for simultaneously interpreting 3-D seismic horizons and faults: Journal of Geophysical Research: Solid Earth, **126**, e2021JB021882, doi: 10.1029/2021JB021882.

De Groot, P., G. de Bruin, and N. Hemstra, 2006, How to create and use 3D Wheeler transformed seismic volumes: 76th Annual International Meeting, SEG, Expanded Abstracts, 1038–1042, doi: 10.1190/1.2369690.

Dorn, G. A., 2010, Visualization and interpretation in 3D — True volume interpretation: First Break, **28**, 87–92, doi: 10.3997/1365-2397.28.3.38387.

Dorn, G. A., 2011, Interpretation workflows enabled by a domain transform: First Break, **29**, 99–108, doi: 10.3997/1365-2397.29.10.55669.

Fehmers, G. C., and C. F. Höcker, 2003, Fast structural interpretation with structure-oriented filtering: Geophysics, **68**, 1286–1293, doi: 10.1190/1.1598121.

Felzenszwalb, P., and D. Huttenlocher, 2012, Distance transforms of sampled functions: Theory of Computing, **8**, 415–428, doi: 10.4086/toc.2012.v008a019.

Geng, Z., X. Wu, Y. Shi, and S. Fomel, 2020, Deep learning for relative geologic time and seismic horizons: Geophysics, **85**, no. 4, WA87–WA100, doi: 10.1190/geo2019-0252.1.

Hale, D., 2009, Structure-oriented smoothing and semblance: CWP Report, **635**, 261–270.

Hale, D., 2011, Structure-oriented bilateral filtering of seismic images: 81st Annual International Meeting, SEG, Expanded Abstracts, 3596–3600, doi: 10.1190/1.3627947.

Hardage, B. A., R. L. Remington, and P. E. Murray, 2007, Reflections have a "Tipper point": AAPG Explorer, 32–35.

He, Y., 2017, Seismic chronostratigraphy for reservoir characterization: Modeling and applications: PhD thesis, University of Texas at Austin.

He, Y., C. Kerans, H. Zeng, X. Janson, and S. Z. Scott, 2019, Improving three-dimensional high-order seismic-stratigraphic interpretation for reservoir model construction: An example of geostatistical and seismic forward modeling of Permian San Andres shelf-Grayburg platform mixed clastic-carbonate strata: AAPG Bulletin, **103**, 1839–1887, doi: 10.1306/11211817244.

Lawrence, T. D., and M. Doyle, 1990, Stratigraphic simulation of sedimentary basins: Concepts and calibration: AAPG Bulletin, **74**, 273–295, doi: 10.1306/0C9B22C7-1710-11D7-8645000102C1865D.

Ligtenberg, H., G. De Bruin, N. Hemstra, and C. Geel, 2006, Sequence stratigraphic interpretation in the Wheeler transformed (flattened) seismic domain: 68th Annual International Conference and Exhibition, EAGE, Extended Abstracts, doi: 10.3997/2214-4609.201402337.

Lomask, J., A. Guitton, S. Fomel, J. Claerbout, and A. A. Valenciano, 2006, Flattening without picking: Geophysics, **71**, no. 4, P13–P20, doi: 10.1190/1.2210848.

Monniron, M., S. Frambati, S. Quillon, Y. Berthoumieu, and M. Donias, 2016, Seismic horizon and pseudo-geological time cube extraction based on a riemmanian geodesic search: IEEE 12th Image, Video, and Multidimensional Signal Processing Workshop, 1–5.

Stafleu, J., and M. D. Sonnenfeld, 1994, Seismic models of a shelf-margin depositional sequence: Upper San Andres Formation, Last Chance Canyon, New Mexico: Journal of Sedimentary Research, **64**, 481–499, doi: 10.1306/D4267FEB-2B26-11D7-8648000102C1865D.

Stark, T. J., 2003, Unwrapping instantaneous phase to generate a relative geologic time volume: 73rd Annual International Meeting, SEG, Expanded Abstracts, 1707–1710, doi: 10.1190/1.1844072.

Stark, T. J., 2004, Relative geologic time (age) volumes — Relating every seismic sample to a geologically reasonable horizon: The Leading Edge, **23**, 928–932, doi: 10.1190/1.1803505.

Stark, T. J., 2005a, Generation of a 3D seismic "Wheeler Diagram" from a high-resolution age volume: 75th Annual International Meeting, SEG, Expanded Abstracts, 782–785, doi: 10.1190/1.2148275.

Stark, T. J., 2005b, System for multi-dimensional data analysis: US Patent 6,850,845.

Stark, T. J., 2006, Visualization techniques for enhancing stratigraphic inferences from 3D seismic data volumes: First Break, **24**, 75–85, doi: 10.3997/1365-2397.24.1094.26926.

Tipper, J. C., 1993, Do seismic reflections necessarily have chronostratigraphic significance? Geological Magazine, **130**, 47–55, doi: 10.1017/S0016756800023712.

Todd, R. G., 1976, Oolite-bar progradation, San Andres Formation, Midland Basin, Texas: AAPG Bulletin, **60**, 907–925, doi: 10.1306/C1EA35DC-16C9-11D7-8645000102C1865D.

Vail, P. R., R. G. Todd, and J. B. Sangree, 1977, Seismic stratigraphy and global changes of sea level. Part 5: Chronostratigraphic significance of seismic reflections: Section 2. Application of seismic reflection configuration to stratigraphic interpretation: M 26, *in* C. E. Payton, ed., Seismic stratigraphy — Applications to hydrocarbon exploration: AAPG Memoirs, 99–116.

Van Vliet, L. J., and P. W. Verbeek, 1995, Estimators for orientation and anisotropy in digitized images, *in* J. van Katjweik, ed., Proceedings of the First Annual Conference of the Advanced School for Computing and Imaging, 442–450.

Weickert, J., 1997, A review of nonlinear diffusion filtering, *in* B. ter Haar Romeny, L. Florack, and J. Koenderink and M. Viergever, eds., Scale-space theory in computer vision: Springer, 1–28.

Wilson, T., M. Handke, D. Loughry, L. Waite, and B. Lowe, 2019, Regional geologic characterization of the Grayburg-San Andres reservoir for salt water disposal management, Midland Basin, Texas: Unconventional Resources Technology Conference, AAPG/SEG/SPE, doi: 10.15530/urtec-2019-902.

Wu, X., and S. Fomel, 2018, Least-squares horizons with local slopes and multigrid correlations: Geophysics, **83**, no. 4, IM29–IM40, doi: 10.1190/geo2017-0830.1.

Wu, X., and D. Hale, 2013, Extracting horizons and sequence boundaries from 3D seismic images: 83rd Annual International Meeting, SEG, Expanded Abstracts, 1440–1445, doi: 10.1190/segam2013-0296.1.

Wu, X., and D. Hale, 2015a, 3D seismic image processing for unconformities: Geophysics, **80**, no. 2, IM35–IM44, doi: 10.1190/geo2014-0323.1.

Wu, X., and D. Hale, 2015b, Horizon volumes with interpreted constraints: Geophysics, **80**, no. 2, IM21–IM33, doi: 10.1190/geo2014-0212.1.

Wu, X., Y. Li, and P. Sawasdee, 2022, Toward accurate seismic flattening: Methods and applications: Geophysics, **87**, no. 5, IM177–IM188, doi: 10.1190/geo2021-0662.1.

Wu, X., S. Luo, and D. Hale, 2016, Moving faults while unfaulting 3D seismic images: Geophysics, **81**, no. 2, IM25–IM33, doi: 10.1190/geo2015-0381.1.

Wu, X., and G. Zhong, 2012, Generating a relative geologic time volume by 3D graph-cut phase unwrapping method with horizon and unconformity constraints: Geophysics, **77**, no. 4, O21–O34, doi: 10.1190/geo2011-0351.1.

Xue, Z., X. Wu, and S. Fomel, 2018, Predictive painting across faults: Interpretation, **6**, no. 2, T449–T455, doi: 10.1190/INT-2017-0171.1.

Zeng, H., M. M. Backus, K. T. Barrow, and N. Tyler, 1998a, Stratal slicing, Part I: Realistic 3-D seismic model: Geophysics, **63**, 502–513, doi: 10.1190/1.1444351.

Zeng, H., Y. He, C. Kerans, and X. Janson, 2020, Seismic chronostratigraphy at reservoir scale: Lessons from a realistic seismic modeling of mixed clastic-carbonate strata in the Permian Basin, West Texas and New Mexico, USA: Interpretation, **8**, no. 1, T13–T25, doi: 10.1190/INT-2019-0053.1.

Zeng, H., S. C. Henry, and J. P. Riola, 1998b, Stratal slicing, Part II: Real 3-D seismic data: Geophysics, **63**, 514–522, doi: 10.1190/1.1444352.

Zeng, H., and C. Kerans, 2003, Seismic frequency control on carbonate seismic stratigraphy: A case study of the Kingdom Abo sequence, west Texas: AAPG Bulletin, **87**, 273–293, doi: 10.1306/08270201023.

Zinck, G., M. Donias, J. Daniel, S. Guillon, and O. Lavialle, 2013, Fast seismic horizon reconstruction based on local dip transformation: Journal of Applied Geophysics, **96**, 11–18, doi: 10.1016/j.jappgeo.2013.06.010.

Biographies and photographs of the authors are not available.